A magnetic phantom technique for investigating structural effects on quantitative ultrasound parameters

Cyril Malinet, Pauline Muleki-Seya, Hervé Liebgott, Jonathan Mamou

A magnetic phantom technique for investigating structural effects on quantitative ultrasound parameters

Cyril Malinet,[1] Pauline Muleki-Seya,[1] Hervé Liebgott,[1] and Jonathan Mamou[2, a]

[1] *Université de Lyon, CREATIS, CNRS UMR 5220, Inserm U1044, INSA-Lyon, Université Lyon 1, Lyon, France*

[2] *Weill Cornell Medicine, Department of Radiology, New York, NY, USA*

(Dated: 19 April 2024)

ABSTRACT

Media that contain ultrasound scatterers arranged in a regular spatial distribution can be considered as structured. Structural effects affect quantitative ultrasound parameters that reflect the microstructure properties. Prior studies examined structural effects using simulations or phantoms with fixed microarchitecture, focusing on a limited set of ultrasound parameters with limited attention given to their underlying physical significance. This study aims to investigate the concordance of the physical interpretations of multiple quantitative ultrasound parameters experimentally by introducing a phantom type with an adjustable microarchitecture. The phantom consists in an aqueous solution containing superparamagnetic microspheres, acting as scatterers. The spatial arrangement of the magnetic particles is modified by applying an external magnetic field, therefore changing the degree of structure of the phantom. Quantitative ultrasound parameters are estimated in three different configurations: the magnetic field intensity is varied over time, strength and orientation. In each experiment, the backscatter coefficient and the envelope quantitative ultrasound parameters are successfully extracted ($R^2 \approx 0.94$). Their physical interpretations are supported by microphotographs and geometrical considerations through concordant hypotheses. This study paves the way for the use of magnetic phantoms. This methodology could be followed to validate theoretical scattering models and the physical meanings of quantitative ultrasound parameters.

[a]cyril.malinet@outlook.com

I. INTRODUCTION

Quantitative ultrasound (QUS) methods aim to extract tissue microstructure information that is pertinent for diagnostic purposes (Oelze and Mamou, 2016). In these methods, theoretical scattering models are applied to the ultrasound backscattered signals measured from a biological sample to estimate the scatterer parameters, such as their sizes or their acoustic properties for instance. The Backscatter Coefficient (BSC) and Envelope Statistics (ES) parametrization are two QUS methods that lead to scattering parameters of different nature. The BSC represents the tissue's ability to backscatter the acoustic energy as a function of the ultrasound frequency (Garcia-Duitama *et al.*, 2015). While the BSC parametrization extracts spectral-based QUS parameters, ES parametrization entails in determining the statistical attributes of the envelope of the temporal backscattered signals. Certain QUS parameters can carry a straightforward physical meaning under specific conditions. For instance, the effective scatterer diameter, derived after applying the Spherical Gaussian model on the experimental BSC, can be related to the size of cellular structures (Insana *et al.*, 1992). In this strict sense, this model can be applied in an isotropic medium where the scatterers are randomly and independently located (*i.e.*, sparse) under multiple approximations, such as Born, far-field, and incident plane waves (Wagner *et al.*, 1990). More generally, the scatterer number density is of prime importance in the correct modeling of the backscattered signals. Indeed, it is reasonable to assume that the correlation of the scatterer position increases with the scatterer concentration (Han and O'Brien, 2015). When the considered medium is not sparse, the medium can be considered as structured.

In structured media, the BSC includes a coherent component and is no longer the incoherent sum of individual scatterer contributions. Similarly, the envelope of Radio-Frequency (RF) signals is affected by the periodic spacing between scatterers (Saha and Kolios, 2011). In biological tissues, cellular structures such as cells can be associated with moderate to high scatterer volume fractions (generally above 0.03)(Franceschini and Guillermin, 2012; Muleki-Seya *et al.*, 2016). Thus, certain biological tissues can be considered as concentrated media in which structural effects need to be taken into account for correctly modeling the scattering of ultrasound waves.

Saha et al. (Saha and Kolios, 2011) studied the effects of different scatterer spatial organizations on spectral and envelope QUS parameters. They simulated four different media, composed of identical scatterers with a decreasing spatial organization that spans from a perfect lattice structure to a random distribution. They restricted the study of the signal envelope to the Rayleigh and the Nakagami distributions. They concluded that the scatterer spatial organization affects the BSC linear slope, the integrated BSC and the envelope QUS parameters. However, they did not investigate the extent to which the physical meaning of the parameters could justify the observed variations. Additionally, this study was restricted to two-dimensional (2D) simulations and did not include an experimental phantom validation.

Several quantitative ultrasound studies that investigated the mean scatterer spacing (MSS) reported the use of structured phantoms. The MSS refers to the average spacing of quasi-periodic scatterers that give rise to a coherent component (Sommer *et al.*, 1981). Weng et al. (Weng *et al.*, 1992) and Narayanan et al. (Narayanan *et al.*, 1997) reported the

use of a phantom that consisted in layers of artificial gel sheets of thickness 0.448 mm. The layers were separated by glass beads randomly located that aimed to generate incoherent backscattering echoes. In this case, the MSS was equal to the layer thickness. Other studies reported the use of arrays of nylon fibers regularly spaced(Kauati *et al.*, 2018), that could be included in a gel that contained randomly distributed glass beads for generating incoherent scattering (Pereira *et al.*, 2002; Rosado-Mendez *et al.*, 2013). Pereira et al. (Pereira *et al.*, 2002) also used homogeneous sponges of different densities, considering the pores as quasi-periodic scatterers. Huang et al.(Huang *et al.*, 2000) used another type of phantom that consisted in a matrix with fluid-filled cylindrical holes distributed with different densities throughout the material. All these phantoms had a fixed geometry and most of them probably required a careful design for the scatterers to exhibit regular tiny spacing. It is noteworthy that MSS was also used as a QUS parameter for tissue characterization in numerous *in vivo* studies (Zhou *et al.*, 2017). MSS-related analyses mostly involved low-frequency insonifications (about 5 MHz), and extracted MSS values that were about 1 mm. Although these studies involved experimental phantom validations, they did not investigate the BSC parametrization and the ES.

Han et al. (Han and O'Brien, 2015) carried out a cell pellet phantom study in which they isolated the structural effects on the BSC using dense phantoms and sparse phantoms containing the same cell lines. After estimating the incoherent BSCs and the total BSCs on each sample, they extracted the structure factors for each cell line by computing their ratio. The estimated structure factors were successfully described by their theoretical models. This study reported an experimental demonstration of the spectral effects of the scatterer

spatial correlation in dense media. One could note that the structural effects resulted from the high cellular concentrations of the biophantoms.

In the present study, the structural effects were investigated on BSC-based and envelope QUS parameters using a novel phantom technique at high frequencies (11 - 41 MHz). The phantom was composed of magnetic microspheres suspended in an aqueous solution. The spatial organization of the particles was modified using a surrounding magnetic field, thus allowing the microarchitecture of the phantom to follow different patterns. The objective of this study is twofold: (1) introducing a new phantom design method to study structural effect and (2) studying the concordance of the physical interpretations of multiple QUS parameters. First, light microscopy measurements were conducted to ensure that the microspheres followed the expected dynamics through an external magnetic field. Then, the variations in the BSC linear slope S and intercept I (Lizzi-Feleppa QUS parameters) were investigated as the phantom microarchitecture was varied. Similarly, the evolutions of envelope QUS parameters were also analyzed. The Homodyned-K distribution was chosen for its capability to model a wide variety of scattering situations (highly variable number of scatterers per resolution cell and quantification of the coherent component) (Cristea *et al.*, 2020; Mamou *et al.*, 2011). The Nakagami distribution was used as its QUS parameters can also carry a physical interpretation. These QUS parameters were estimated as the magnetic field intensity varied over time, strength and directions in three distinct experiments. The physical meanings of these QUS parameters and their concordance were investigated. This

new type of magnetic phantom could be used by the ultrasound community to validate theoretical scattering models in structured media.

II. METHOD

A. Superparamagnetic beads

In this study, a phantom composed of superparamagnetic beads was used. These microspheres are highly monodisperse (coefficient of variation 1.1%) with a diameter of 10 µm (Sigma-Aldrich, ref. 49664) and are suspended in water with a volume fraction equal to 0.028. The particles consist of a polystyrene polymer matrix in which nanometric iron oxide particles are homogeneously incorporated ($> 20\%$), which gives them superparamagnetic properties. In the simulations carried out in this study, the bead sound speed was set to 2400 m/s and the Poisson coefficient to 0.34. The bead mass density was set to 1.71 g/cm^3 (supplier data).

1. Expected bead dynamics

The magnetic beads show no specific interaction when no surrounding magnetic field is applied. However, when the beads are placed in a magnetic field $\vec{B}$, they behave like magnetic dipoles and exhibit a magnetic moment $\vec{M}$. This phenomenon is known as paramagnetism.

The hysteresis is the delayed response of ferromagnetic materials to changing magnetic fields. The superparamagnetic beads exhibit a limited magnetic hysteresis in comparison to

paramagnetic beads. Thus, the superparamagnetic beads can find their initial magnetization state quickly after a first magnetization compared to paramagnetic beads, which can exhibit a longer "memory". Consequently, superparamagnetic beads were chosen in order to enhance the reproducibility of the experiments over time.

The magnetic dipoles are then subject to a magnetic force $\vec{F}$ that can be expressed as:

$$\vec{F} = \overrightarrow{grad}(\vec{M}.\vec{B}) \tag{1}$$

where $\overrightarrow{grad}$ represents the gradient operator and . the dot product. As a result, the magnetic force $\vec{F}$ tends to align the magnetic dipoles along magnetic field lines of $\vec{B}$. A secondary induced magnetic field is then exhibited by every bead, as depicted in Figure 1. Consequently, the beads act as secondary magnets and are therefore modeled as individual pairs of north and south poles. Because the north and south poles of two different beads are attracted, the beads form chains along the surrounding magnetic field lines. Thus, when a uniform stationary surrounding magnetic field $\vec{B}$ is present, the superparamagnetic beads are expected to arrange themselves into parallel stationary chains along the orientation of the magnetic field as depicted in Figure 2 (a, b). This bead configuration can be obtained using solid magnets and coils. Indeed, the magnetic field within the region which is equidistant to the north and the south poles of two neighboring bar magnets can be considered uniform to a certain extent. The same observation can be made about the magnetic field located in the center of a coil subjected to a continuous current. In practice, the solid magnets and the coils used in this study are assumed large enough relatively to the magnetic phantom size to obtain the required field uniformity (at least five times larger).

The chains exhibit equidistant spacing in the direction perpendicular to the surround-

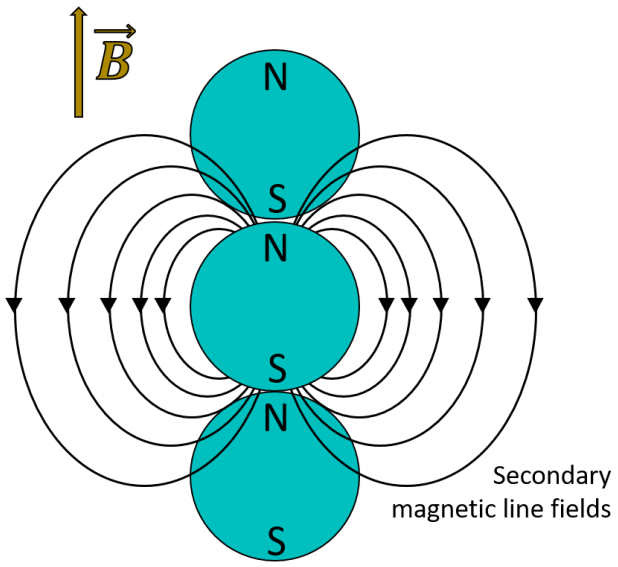

FIG. 1. Secondary magnetic field lines from a single magnetic bead. N and S stand for the north and the south poles respectively. The external magnetic field is depicted with the vector $\vec{B}$

ing magnetic field $\vec{B}$ due to their repelling line fields. This distance is characteristic of the magnetic repulsion.

2. Light microscopy measurements

Light microscopy measurements were performed to verify the theoretical bead dynamics mentioned in the previous section. To do so, droplets of the phantom solution were put on glass slides with no coverslip. Firstly, the dynamics of the beads were observed over time under a microscope when the magnetic field intensity instantaneously increased from 0 mT to 4 mT. To create a homogeneous horizontal stationary magnetic field, two neodymium

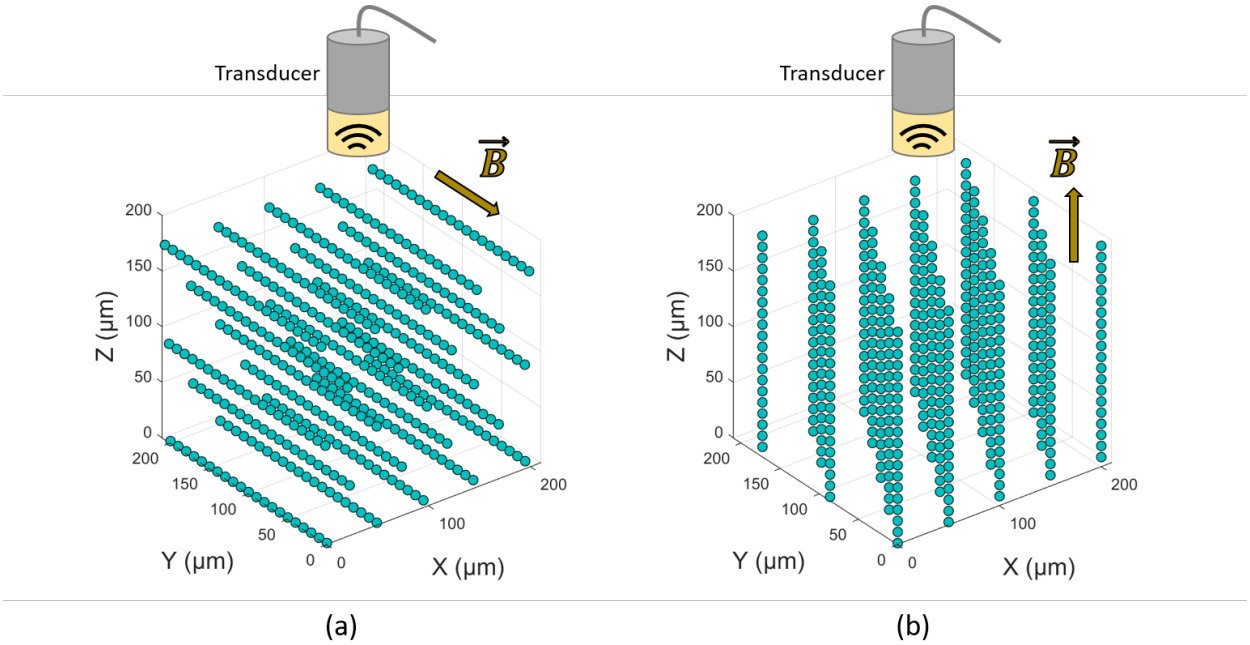

FIG. 2. Bead alignment in the presence of a homogeneous stationary magnetic field. (a) Horizontal configuration used in experiments 1 and 2. (b) Vertical configuration used in experiment 3. For each configuration, the ultrasound transducers were depicted (not on scale) to clarify the directions.

block magnets (N52, BY JMY) of dimension 40 x 40 x 20 mm were manually quickly placed across the glass slide at $t = 3$ s, where t represents the time. The distance between the two permanent magnets was 19.6 cm and was set such that the magnetic field intensity at the droplet location equals 4 mT. The spacing between the magnets was measured with a caliper and the intensity was confirmed with a teslameter (Naroote). A RGB camera captured the bead dynamics over 9 seconds (100 frames per second). Secondly, the RGB camera captured snapshots of droplets of the phantom solution at $t = 9$ s under a magnetic field intensity of 19 mT by reducing the spacing between the two magnets to 15.7 cm.

B. Experimental setups

In all experiments, a spherically focused single-element transducer (PI-50-T2, Panametrics) with a focal distance of 19 mm and an aperture of 6.3 mm (*i.e.*, F-number of 3) scanned the phantom solution with a motorized platform. Its -6 dB bandwidth spanned from 11 MHz to 41 MHz with a center frequency of 26 MHz. The transducer was excited by a Panametrics 5900 pulser/receiver unit (Olympus NDT, Waltham, MA, USA) used with an energy setting of 32 µJ in the pulse-echo mode. The wave propagation direction was set to the vertical of the laboratory (*i.e.*, Z-axis). All the following orientations mentioned in this study are defined relative to this reference direction. The axial resolution R_{ax} and the lateral resolution R_{lat} were estimated to $R_{ax} = 26$ µm and $R_{lat} = 173$ µm.

To mitigate the effect of the phantom attenuation prior to the focal point of the transducer, a low-attenuating block of agar gel was placed between the transducer and the phantom solution. The agar-gel block was mostly composed of water and had an agar concentration of 0.7%. The thickness of this block (18 mm) was chosen to position the focal point of the transducer immediately following the interface between the agar and phantom solution.

1. Experiment 1

The first experiment investigates the QUS parameter variations when the chains of beads are horizontal (*i.e.*, normal to the ultrasound propagation direction, Figure 2, a). This

experiment is referred to as experiment 1 and is described in Figure 3. The phantom solution was gently manually stirred prior to data acquisition. In the first three seconds, the magnetic beads were randomly located, as no surrounding magnetic field was applied. To create a homogeneous horizontal stationary magnetic field, the two permanent magnets were placed across the phantom solution at $t = 3$ s, similarly to what was done for light-microscopy imaging. The measurements start 3 seconds before the bead magnetization to capture the QUS parameters dispersions with no external magnetic field. The distance between the two permanent magnets was 19.6 cm such that the magnetic field intensity at the phantom location was equal to 4 mT.

In this experiment, the single-element transducer scanned the same phantom area along the Y-axis over 6.7 mm by going back and forth, therefore generating a one-dimensional (1D) scan every second. QUS parameters were then extracted for each scan from a unique ROI with dimensions equal to 15.6λ (0.9 mm) and 116λ (6.7 mm) in the axial and the lateral direction respectively. The width of the ROI was taken as large as the lateral displacement of the transducer to increase the robustness of the corresponding QUS parameters, given that the sample was a phantom that could exhibit limited heterogeneities. Experiment 1 was repeated six times (*i.e.* 6 independent 1D scans for each second). Between the experiments, the phantom was stirred in the absence of a surrounding magnetic field to redistribute the beads in their initial random spatial distribution. The last measurements occurred 6 seconds after the magnets were placed.

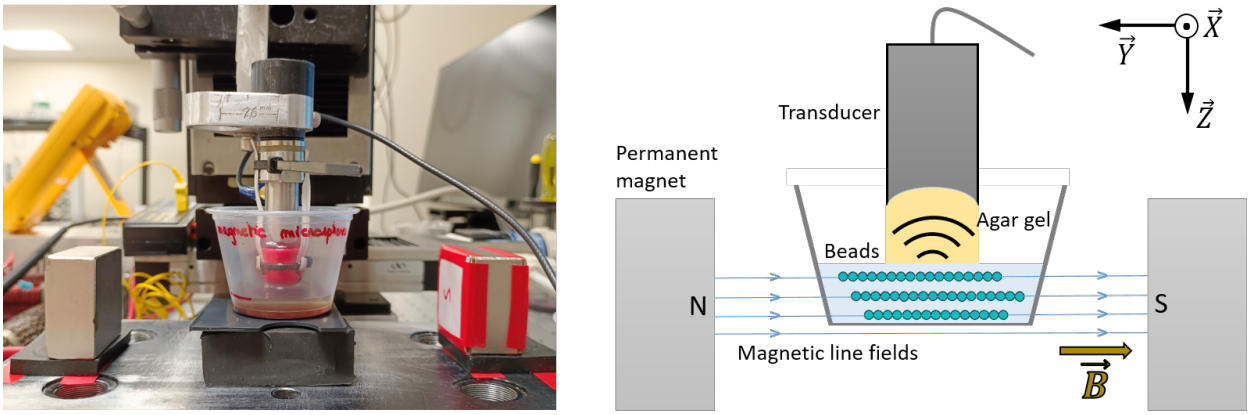

FIG. 3. Horizontal configuration: experiments 1 and 2. (a) Picture of the experimental setup. (b) Explanatory scheme. N and S stand for the north and the south poles respectively.

2. Experiment 2

The second experiment also investigates QUS parameter variations when the chains of beads are horizontal but is focused on the intensity of the magnetic field (Figure 2, a). This experiment is referred to as experiment 2 and necessitates the same experimental setup as in experiment 1 (Figure 3, a). The magnets were placed across the phantom and the 1D scan along the Y-axis over 11.3 mm occurred 6 seconds after the placement of the magnets. Six magnetic field intensities were obtained by varying the spacing between the two magnets (0 mT, 4 mT, 8 mT, 11 mT, 15 mT and 19 mT). QUS parameters were then extracted for each scan from a unique ROI with dimensions equal to 15.6λ (0.9 mm) and 196λ (11.3 mm) in the axial and the lateral direction respectively. In this case, the dimension of the ROI in the lateral direction was longer than in Experiment 1 because the scan duration did not have to equal 1 second. Wider ROIs make the estimation of QUS parameters more robust

as a result due to their stochastic nature. This experiment was repeated 10 times (*i.e.*, 10 independent 1D scans per intensity). Similarly, the phantom solution was stirred between the different acquisitions.

3. Experiment 3

The third experiment studies the QUS parameter variations when the chains are vertical (Figure 2, b). This experiment is referred to as experiment 3 and is described in Figure 4. The phantom solution was placed in a coil that generated a homogeneous stationary vertical magnetic field when it carried a continuous current. The coil was specifically designed for this experiment and had 55 spires of copper wire. The coil's length is 13 cm and its inner diameter is 4 cm. The coil was put in series with a 24 V power supply and an adjustable resistance that can reach 0.1 Ohm (E300K1R0E, Ohmite). The resistor used is suitable for high-power applications (up to 300 W). As the resistance decreases, both the current and magnetic field intensity increase. A 1D scan along the Y-axis over 6.7 mm was acquired 6 seconds after the power supply was turned on. Four different magnetic field intensities were obtained by varying the current intensity from 7.2 A to 34.6 A. This experiment was repeated 3 times (*i.e.*, 3 independent 1D scans per intensity). Similarly, the phantom solution was stirred between the acquisitions.

To obtain more QUS parameters than the number of scans, QUS parameters were extracted from ROIs that were 15.6λ (0.9 mm) long in the axial direction and 17λ (0.98 mm) long in the lateral direction with an overlapping equal to 50% along the lateral direction only. As a result, 39 data points were obtained for each magnetic field intensity for each

parameter. The choice of working with smaller ROIs in the lateral direction results from the lower number of 1D scans obtained for this experiment due to the lengthy acquisition procedure.

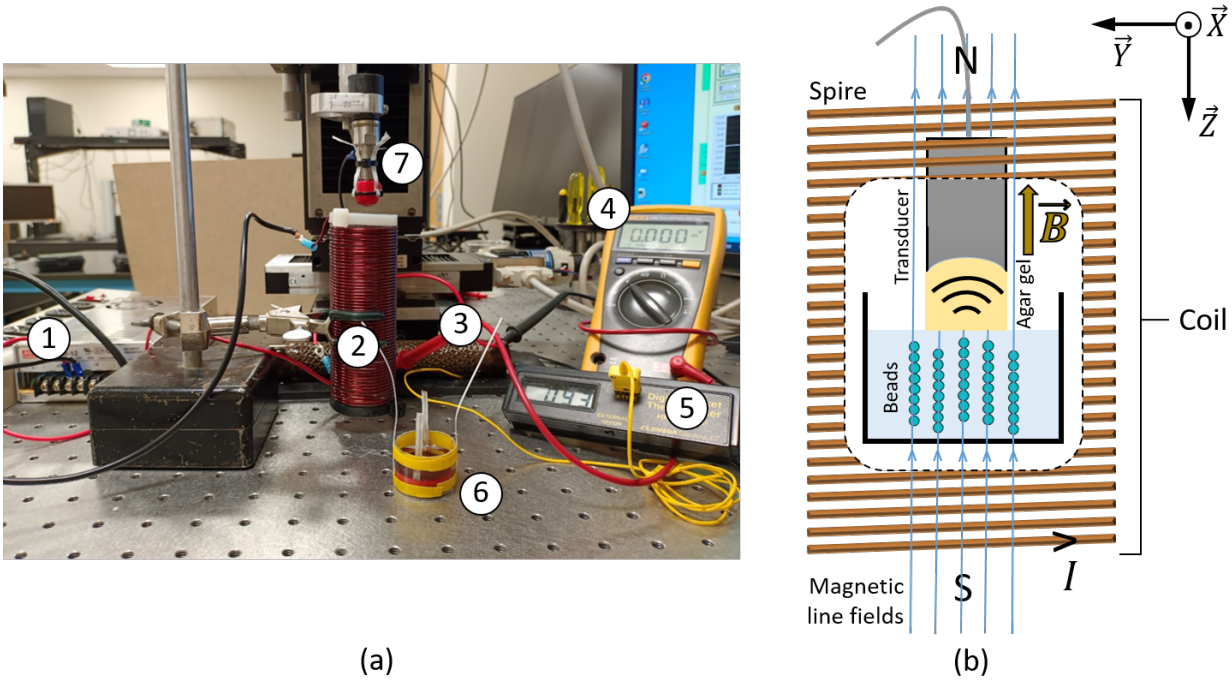

FIG. 4. Experiment 3: vertical configuration. (a) Picture of the experimental setup. The power supply (1) is in series with the coil (2) and the adjustable resistor (3). A voltmeter (4) in parallel to the resistor measures the intensity that flows through the coil. A thermometer checks the temperature to avoid overheating. The phantom solution (6) is placed inside the coil when the transducer (7) performs a 1D scan. (b) Explanatory scheme of the coil. N and S stand for the north and the south poles respectively.

The specificities of each ultrasound experiment are summed up in Table I.

	Experiment 1	Experiment 2	Experiment 3
Magnetic field variation	Temporal	Amplitude	Amplitude
Magnetic field direction*	Horizontal	Horizontal	Vertical
Method to generate magnetic field	Solid magnets	Solid magnets	Coil

TABLE I. Description of the three ultrasound experiments. *The vertical direction is the wave propagation direction (*i.e.*, Z-axis).

C. QUS parameter estimations

In this section, the estimation methods of the QUS parameter are first described. Then, each parameter is introduced along with its physical interpretation and its possible evolution when subjected to a magnetic field.

1. Spectral QUS parameters

a. Estimation. The BSC was estimated using the reference phantom method (Yao *et al.*, 1990) with a reference phantom composed of glass beads with a 4.5 µm diameter suspended in a gel that acoustically behaves like water. The volume fraction was equal to 0.011 and the density of the glass bead was taken equal to 2.5 g/cm^3. The Poisson coefficient was set to 0.2 and the glass bead sound speed to 5640 m/s. The Faran model (Faran Jr, 1951) is chosen to compute the theoretical reference BSC. The magnetic solution attenuation was estimated using a standard substitution method (Kuc and Schwartz, 1979)

in each configuration to take into account potential anisotropic effects. The attenuation of the agar-gel block affects similarly both the magnetic phantom measurements and the reference phantom measurements. Indeed, the same block of agar gel was used for each experiment. Thus, the attenuation of the block of agar-gel is canceled out when calculating the ratio associated with the reference phantom method.

b. Lizzi-Feleppa approach. This approach involves fitting the estimated BSC expressed in dB as a linear function (Lizzi *et al.*, 1987). First, the estimated BSC is normalized by 1 $m^{-1}.sr^{-1}$ to obtain a unitless quantity. This procedure leads to ultrasound parameters known as the Lizzi-Feleppa coefficients: the slope S (dB/MHz), the intercept I (dB) and the midband value M (dB):

$$10log_{10}(BSC) \rightarrow Y_{LF}(f) = S \times f + I \,; M = Y_{LF}(f_{mid}) \tag{2}$$

where $Y_{LF}(f)$ is the resulting linear fit and f_{mid} the middle frequency. Only two out of the three Lizzi-Feleppa QUS parameters are independent. In this study, the slope S and the intercept I are the BSC parameters of interest.

2. Envelope QUS parameters

In this study the probability density function of the envelope signals of each ROI was fitted to Nakagami and Homodyned-K distributions.

a. The Nakagami distribution. The Nakagami distribution can be used to extract the

scaling factor Ω_{nak} and the Nakagami parameter α_{nak}. The scaling factor Ω_{nak} is equivalent to the mean backscattered intensity (Cristea *et al.*, 2020) and α_{nak} can be used to quantify the effective number of scatterers per resolution cell (Cristea *et al.*, 2020; Mamou *et al.*, 2011). If A is a random variable that follows a Nakagami distribution, then its probability density function (PDF) D_{nak} can be written as:

$$D_{nak}(A) = \frac{2\alpha_{nak}^{\alpha_{nak}}}{\Gamma(\alpha_{nak})\Omega_{nak}^{\alpha_{nak}}} A^{2\alpha_{nak}-1} e^{-\alpha_{nak}A^2/\Omega_{nak}} \tag{3}$$

where Γ is the Euler gamma function. The scaling parameters Ω_{nak} and the Nakagami parameter α_{nak} were obtained using a maximum-likelihood estimator.

b. The Homodyned-K distribution. The expression of the PDF of the Homodyned-K (HK) distribution is(Mamou *et al.*, 2011):

$$D_{hk}(A) = A\int_0^\infty xJ_0(s_{hk}x)J_0(Ax)(1+\frac{x^2\sigma_{hk}^2}{2\mu_{hk}})^{-\mu_{hk}}dx \tag{4}$$

where J_0 is the 0^{th}-order Bessel function of the first kind, s_{hk}^2 the coherent signal energy, σ_{hk}^2 the diffuse signal energy and μ_{hk} is somewhat the analogous to the Nakagami parameter α_{nak}. The scatterer clustering QUS parameter μ_{hk}, s_{hk} and σ_{hk} were obtained using the XU estimator(Destrempes *et al.*, 2013).

3. Physical meaning of QUS parameters

The slope S of the linear BSC can be affected by both the incoherent and the coherent components of the BSC. Firstly, the slope S of the incoherent BSC can be correlated to

the effective scatterer diameter (ESD) to a certain extent (Lizzi *et al.*, 1988; Muleki-Seya *et al.*, 2018). Given that the maximum frequency of the transducer is sufficiently high (ka = 0.84 at 40 MHz, k being the wavenumber and a the scatterer radius), the ESD could potentially represent the bead diameter which remains unchanged as the magnetic field intensity increases. Thus, the slope S of the incoherent BSC may be constant under a varying magnetic field. Secondly, a coherent component due to the periodicity of the scatterer's spatial position is expected in the presence of a magnetic field. This coherent component can be taken into account by considering a structure factor that is supposed to exhibit periodic sharp peaks, distant of a characteristic frequency that reflects the scatterer's diameter. These peaks could decrease the goodness of the linear fit but they should have a limited impact on the general trend of the BSC, making the slope S potentially unaffected as well.

Given that the coherent signals may not affect the shape of the BSC as discussed above, the BSC intercept I and Ω_{nak} could reflect the incoherent BSC components. The incoherent BSC is proportional to the scatterer density. In the case of a resolution cell smaller than the repulsive distance, one could hypothesize that a given resolution cell counts more beads compared to the initial random distribution if the resolution cell encompasses a chain. Conversely, a resolution cell could count fewer beads if it is located in the interchain area. In both scenarios, the number of beads could exhibit a monotonous trend: an increase or a decrease. Assuming that the resolution cell continues to populate or depopulate as the chains form, the corresponding monotonic trend in the intercept I and Ω_{nak} could be expected as the magnetic field intensity increases. Predictions about the evolutions of α_{nak}

are given below along with its equivalent parameter from the Homodyned-K distribution.

The ratio $k_{hk} = s_{hk}/\sigma_{hk}$, termed as the coherent-to-diffuse signal ratio, can describe the degree of structure in the scatterer spatial position in the considered ROI. Considering the transition of beads from a random distribution to a highly organized pattern, it is reasonable to anticipate that the coherent-to-diffuse signal ratio k_{hk} will exhibit an increase with rising magnetic field intensity.

The envelope-related coefficients α_{nak} and μ_{hk} can reflect the number of scatterers per resolution cell (*i.e.*, the scatterer density) to a certain extent. In a simulation and a phantom study, Cristea et al.(Cristea *et al.*, 2020) reported a monotonic increase of α_{nak} and μ_{hk} as the number of scatterers per resolution cell increases up to 43 at 22 MHz (*i.e.*, volume fraction of 0.125). These QUS parameters and the scatterer density were no longer correlated beyond this limit. Simulations revealed that the scatterer clustering QUS parameters μ_{hk} were more sensitive than the Nakagami parameter α_{nak} to the scatterer number density after it reaches 10 scatterers per resolution cell. Given the bead concentration and the volume of the resolution cell reported in this study, the number of scatterers per resolution cell was estimated to equal 32 at 26 MHz. Hence, the estimations of α_{nak} and μ_{hk} are expected to correlate with the density of scatterers, with μ_{hk} exhibiting a higher sensitivity.

III. RESULTS

A. Light microscopy measurements

Four successive microphotographs are shown at different times in Figure 5: with no magnetic field (a), $t = 4$ s with magnets (b), $t = 5$ s with magnets (c), $t = 9$ s with magnets (d). The magnetic field intensity equals 4 mT for these images. At $t = 2$ s, the suspended beads are motionless and behave like normal microspheres without specific interaction. One second after the placement of the magnets, the chain formation can be observed along the direction of the magnetic field. A repulsive distance of about two times the bead diameter can be observed along the X-axis. The beads move until $t = 5$ s. At this time, longer and more distant chains appear in comparison to what can be observed at $t = 4$ s. The beads have reached their final positions or exhibit limited displacements after $t = 5$ s.

The microphotograph of magnetic beads at $t = 9$ s under a 19 mT magnetic field (Figure 5, e) reveals the existence of chains that are longer along the Y-axis and more distant along the X-axis in comparison to the chains observed in (d) for 4 mT at the same time.

B. Experiment 1

1. Spectral QUS parameter results

Before delving into the analysis of QUS parameters, the potential impact of multiple scattering was studied through theoretical considerations. A simple configuration involving two neighboring magnetic beads insonified by an incident plane wave is studied, assuming

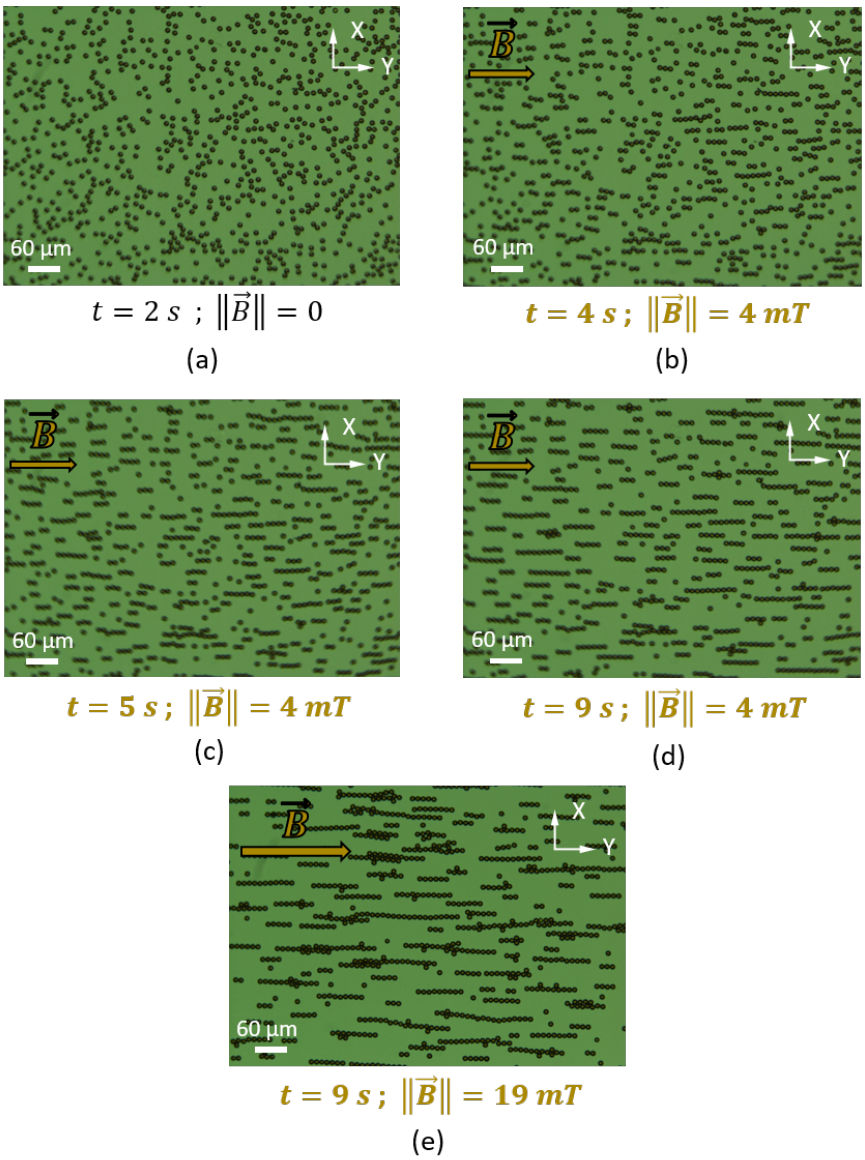

FIG. 5. Microphotographs of superparamagnetic beads captured with no magnetic field (a), $t = 4$ s with magnets (b), $t = 5$ s with magnets (c), $t = 9$ s with magnets (d). The magnetic field intensity equals 4 mT. Images (a),(b), (c) and (d) were acquired successively. Image (e) represents the magnetic beads 6 seconds after the placement of the magnets with a magnetic field intensity equal to 19 mT.

far-field. The Faran theory (Faran Jr, 1951) for elastic scatterers was used. The pressure

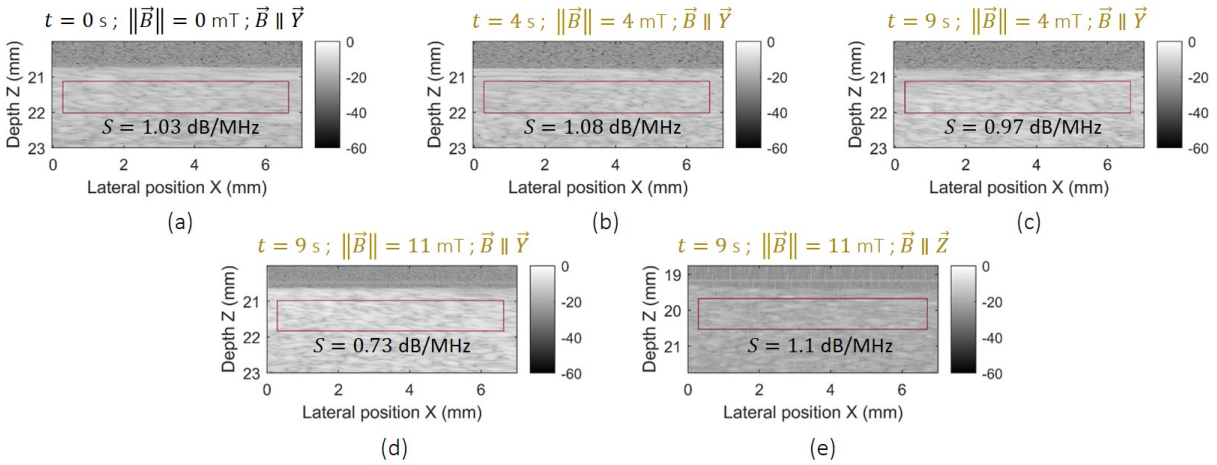

FIG. 6. Illustrative examples of B-mode images. The red rectangle represents the ROI. The slope value of the corresponding linear BSC S is given below. Experiment 1 is depicted through a scan acquired with no magnetic field (a), 1 second after the magnetic field intensity reached 4 mT (b) and 6 seconds after (c). (d) B-mode image corresponding to experiment 2 ($\|\vec{B}\| = 11$ mT, $\vec{B} \parallel \vec{Y}$). (e) B-mode image corresponding to experiment 3 ($\|\vec{B}\| = 11$ mT, $\vec{B} \parallel \vec{Z}$).

intensity in the backscattering direction after two scattering events was found negligible compared to the one of a single backscattering event (ratio less than 1%). Therefore, multiple scattering can be safely disregarded here and in the rest of this study. The attenuations of the reference phantom and of the magnetic phantom in both configurations are estimated to 1.6 dB/mm and to 3.3 dB/mm at 26 MHz respectively.

In experiment 1, the magnets are placed around the phantom solution at $t = 3$ s. Illustrative examples of scans with their corresponding ROI and slope estimations S are given in Figure 6 (a), (b) and (c), before, 1 second after, and 6 seconds after the magnetic field intensity reached 4 mT respectively. The variations of the slope S and the intercept I are shown in Figure 7 (a) and (b) respectively. In all the boxplots, the box displays the

median as its central mark, while its lower and upper boundaries represent the 25^{th} and 75^{th} percentiles, denoted q_1 and q_3 respectively. The continuous line connects the medians. The whiskers extend to the most extreme non-outlier data points. Data points are considered as outliers if they fall outside the range $[q_1 - 3/2(q_3 - q_1), q_3 + 3/2(q_3 - q_1)]$. Outliers are individually depicted using circular symbols.

The slope S increases when the magnets are placed. A fast decay is then observed at $t = 5$ s before stabilizing around relatively low values. The intercept I shows a continuous increase from $t = 3$ s to $t = 6$ s and then reaches a plateau. The goodness of fit R^2 is shown in Figure 7 (c). The same fitting quality is reported for each time (approximately $R^2_{LF} = 0.95$).

2. Envelope QUS parameter results

The second row of Figure 7 shows the Nakagami QUS parameters and the third row displays the Homodyned-K QUS parameters. The scaling parameters Ω_{nak}, the Nakagami QUS parameters α_{nak} and the scatterer clustering QUS parameter μ_{nak} underwent compression using a base-10 logarithm due to their extensive value range. The Nakagami QUS parameters α_{nak} show a quick relative increase when the magnets are placed around the phantom solution (Figure 7, d). The coefficient α_{nak} immediately decreases at $t = 5$ s and stabilizes afterward. The scaling parameter Ω_{nak} exhibits an increase when the magnets are placed (Figure 7, e) before reaching a plateau at $t \approx 5$ s.

Figure 7 (g) shows the variation of the scatterer clustering QUS parameter μ_{hk}. The

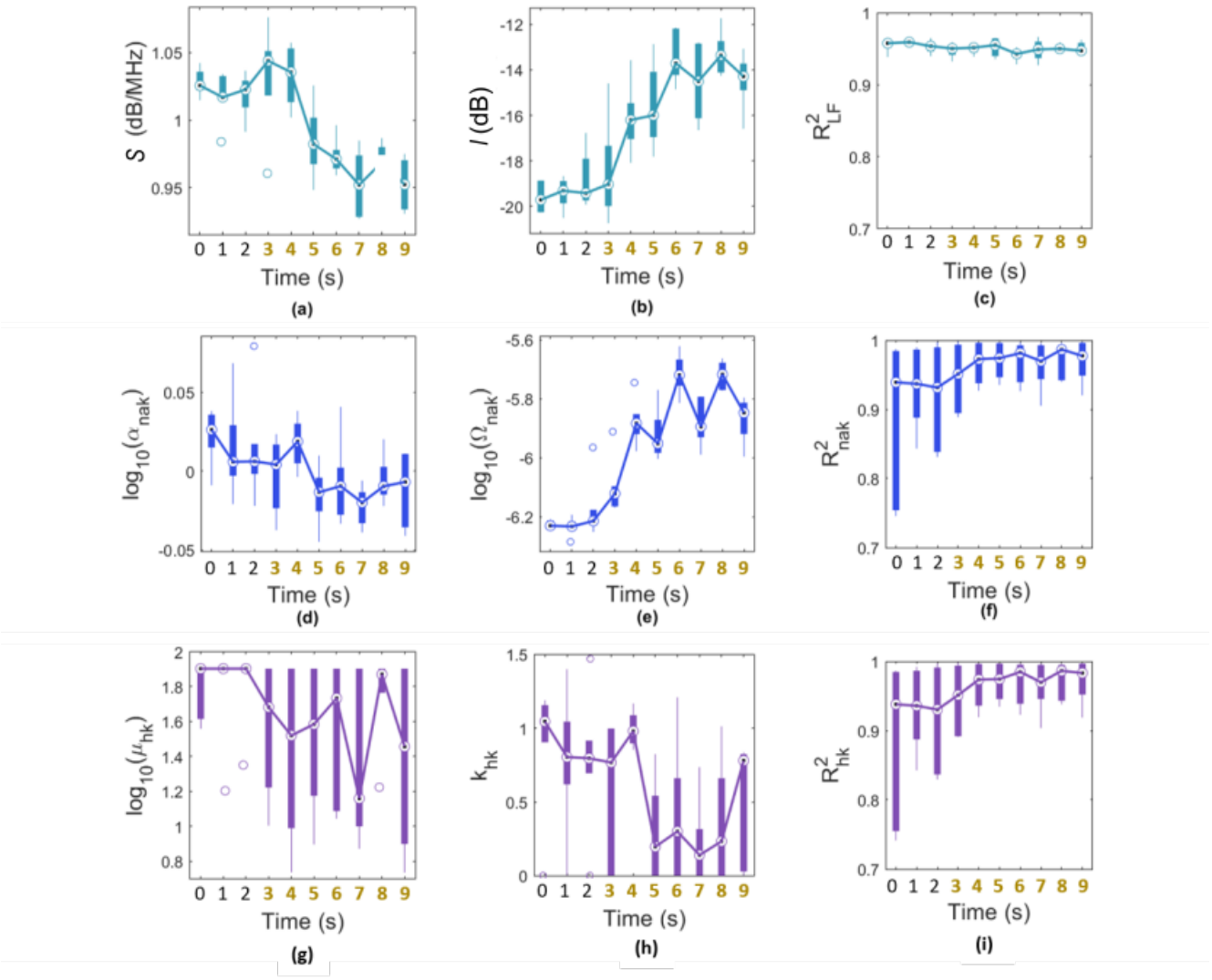

FIG. 7. Experiment 1 results. The first row shows the Lizzi-Feleppa QUS parameters versus time, the second row shows the Nakagami QUS parameters and the third row the Homodyned-K QUS parameters. No magnetic fields were present between $t = 0$ and $t = 2$ s. Bold time values indicate times where the magnetic field equals 4 mT. (a) BSC slope S (b) BSC intercept I. (c) Goodness of the BSC linear fit parameters. (d) Nakagami QUS parameters α_{nak}. (e) Scaling factors Ω_{nak}. (f) The goodness of fit R^2_{nak} for Nakagami distributions. (g) Scatterer clustering QUS parameter μ_{hk}. (h) Coherent to diffuse signal ratio k_{hk}. (i) The goodness of fit R^2_{hk} for Homodyned-K distributions.

384 QUS parameter values for the first three seconds show the presence of data points that have
385 reached the upper bound of the inversion constraint ($\mu_{hk} = 80$). The boxes at other times
386 show extensive ranges of values, making their analysis also limited.

387 The coherent-to-diffuse signal-to-noise ratio k_{hk} increases when the magnets are placed
388 around the phantom (Figure 7, h), followed by a fast decay at $t = 5$ s. The coherent-to-
389 diffuse signal ratio k_{hk} then stabilize at $t = 8$ s.

390 The goodness of fits of the Nakagami and the Homodyned-K distributions show similar
391 trends (Figure 7, f, i). The R^2 coefficients without the magnetic fields (*i.e.*, the first three
392 seconds) exhibit lower values ($R^2 \approx 0.94$) and a broader range in comparison to the other
393 fits ($R^2 \approx 0.97$). Specifically, the very first measurements at $t = 0$ s led to the poorest
394 quality of fits (down to $R^2 = 0.74$).

395 C. Experiment 2

396 *1. Spectral QUS parameter results*

397 In experiment 2, the scans are performed 6 seconds after a horizontal magnetic field
398 intensity was established. An illustrative example of scan with its corresponding slope
399 estimation S is given (Figure 6, d). The variations of the slope S and the intercept I as the
400 magnetic field intensity increases are shown in Figure 8 (a) and (b) respectively. The slope
401 S decreases until 15 mT from 0.82 dB/MHz to 0.67 dB/MHz and exhibits a plateau after.
402 The intercept I shows a continuous increase up to 15 mT and also presents a plateau after.
403 The goodness of fit R^2 is shown in Figure 8 (c). The same fitting quality is reported for

each intensity (approximately $R^2_{LF} = 0.94$).

2. *Envelope QUS parameter results*

The envelope QUS parameters are shown in Figure 8. The Nakagami parameter α_{nak} decreases as $\|\vec{B}\|$ increases (Figure 8, d). The scaling parameter Ω_{nak} exhibits an increase for the first four magnetic field intensities from 6.0×10^{-7} to 1.6×10^{-6} (Figure 8, e) and reaches a plateau after 15 mT.

Figure 8 (g) shows the variation of the scatterer clustering QUS parameter μ_{hk}. The estimations for the first three magnetic field intensities show the presence of data points that have reached the upper bound of the inversion constraint. A decrease is observed from after $\|\vec{B}\| = 8$ mT.

The coherent-to-diffuse signal-to-noise ratio k_{hk} slightly decreases up to 11 mT and exhibits a fast decay at 15 mT (Figure 8, h). The coefficient k_{hk} reaches near-zero values and stabilizes afterward.

The goodness of fits of the Nakagami and the Homodyned-K distributions show similar trends (Figure 8, f, i): the R^2 coefficients are about $R^2 = 0.98$.

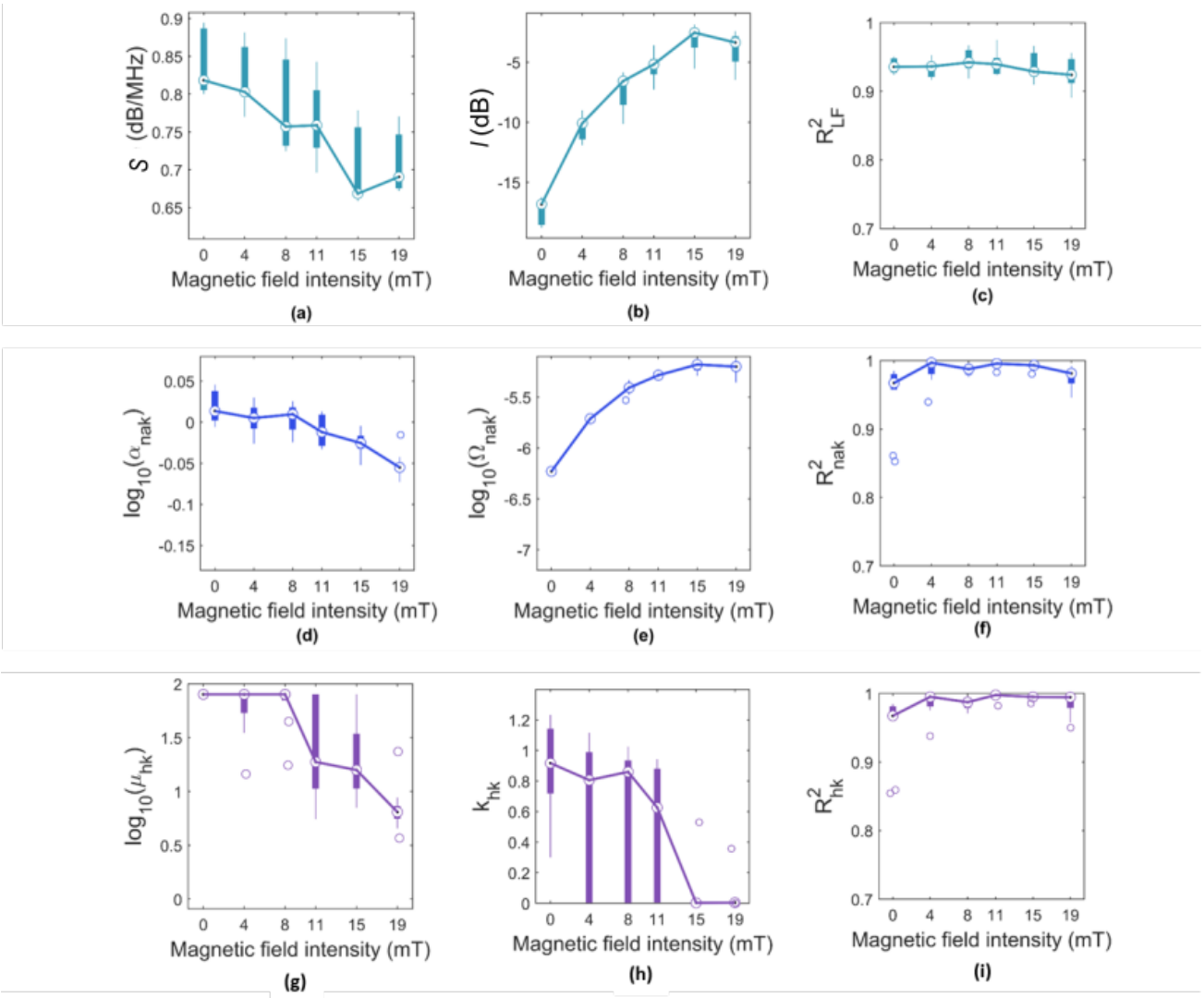

FIG. 8. Experiment 2 results. The first row shows the Lizzi-Feleppa QUS parameters versus magnetic field intensity, the second row shows the Nakagami QUS parameters and the third row the Homodyned-K QUS parameters. (a) BSC slope S (b) BSC intercept I. (c) Goodness of the BSC linear fit parameters. (d) Nakagami QUS parameters α_{nak}. (e) Scaling factors Ω_{nak}. (f) The goodness of fit R^2_{nak} for Nakagami distributions. (g) Scatterer clustering QUS parameter μ_{hk}. (h) Coherent to diffuse signal ratio k_{hk}. (i) The goodness of fit R^2_{hk} for Homodyned-K distributions.

D. Experiment 3

1. *Spectral QUS parameter results*

In experiment 3, the scans are acquired 6 seconds after a vertical magnetic field intensity was established. An illustrative example of scan with its corresponding slope estimation S is given (Figure 6, e). The slope S and the intercept I were extracted following the same procedure as in the previous experiences (Figure 9 (a) and (b) respectively). The slope S increases with the magnetic field intensity except for $\|\vec{B}\| = 8$ mT, where a drop can be observed. The intercept I decreases except for $\|\vec{B}\| = 8$ mT. The goodness of fit R^2 is shown in Figure 9 (c). The R^2_{LF} coefficients for $\|\vec{B}\| = 8$ mT exhibit lower values in comparison to the other fits (about $R^2_{LF} = 0.86$ versus $R^2_{LF} = 0.92$).

2. *Envelope QUS parameter results*

The envelope QUS parameters are shown in Figure 9. The Nakagami parameter α_{nak} tends to decrease with the vertical magnetic field intensity (Figure 9, d). The scaling parameter Ω_{nak} exhibits a decrease as $\|\vec{B}\|$ increases except for = 8 mT (Figure 9, e).

Figure 9 (g) shows the variation of the scatterer clustering QUS parameter μ_{hk}. The distribution of data points at 0 mT shows the presence of QUS parameters that have reached the upper bound of the inversion constraint. The same trends as described for the Nakagami parameter α_{nak} can be observed. However, the relative variations between QUS parameters are greater in this case. The coherent-to-diffuse ratio k_{hk} shows a broad range of values for each magnitude of the vector field $\|\vec{B}\|$ (Figure 9, g). As a result, no clear trend can be

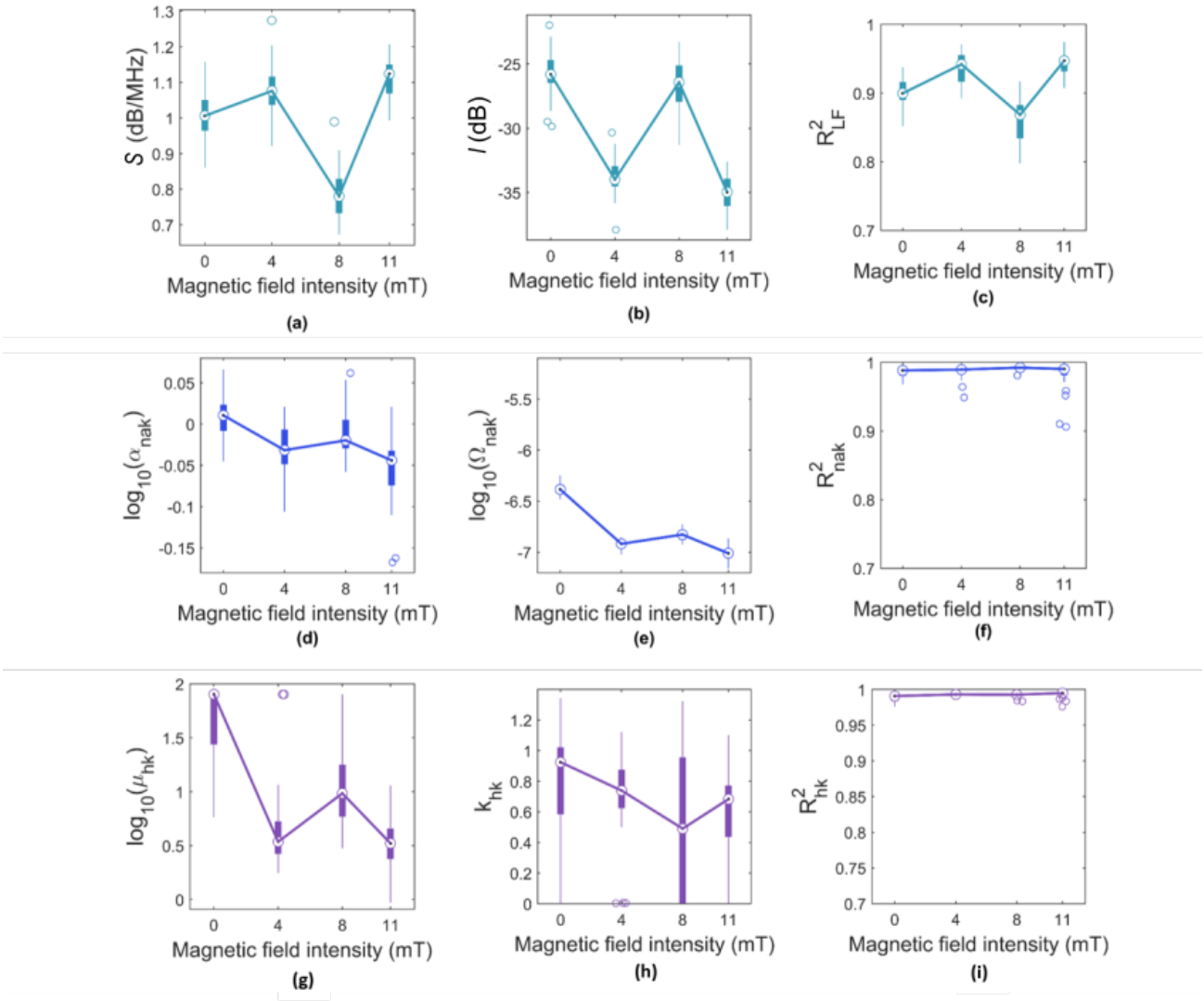

FIG. 9. Experiment 3 results. The first row shows the Lizzi-Feleppa QUS parameters versus magnetic field intensity, the second row shows the Nakagami QUS parameters and the third row the Homodyned-K QUS parameters. (a) BSC slope S (b) BSC intercept I. (c) Goodness of the BSC linear fit parameters. (d) Nakagami QUS parameters α_{nak}. (e) Scaling factors Ω_{nak}. (f) The goodness of fit R^2_{nak} for Nakagami distributions. (g) Scatterer clustering QUS parameter μ_{hk}. (h) Coherent to diffuse signal ratio k_{hk}. (i) The goodness of fit R^2_{hk} for Homodyned-K distributions.

identified.

The goodness of fits of the Nakagami and the Homodyned-K distributions show similar trends (Figure 9, f, i) and approximately equal $R^2 = 0.99$.

IV. DISCUSSION

This study aims to investigate and combine the physical interpretations of QUS parameters experimentally by introducing a new phantom type. This approach benefits from the magnetic properties of superparamagnetic beads to isolate the effects of a specific scatterer organization on the scattering signals.

To do so, QUS parameters were estimated in a phantom solution composed of superparamagnetic beads in different magnetic field configurations. The magnetic field intensity was varied over time, strength and orientation in three distinct experiments.

Firstly, in experiment 1, the magnetic field was horizontal (Y-axis) and induced by the placement of two solid magnets across the phantom solution (Figure 3). The beads were instantaneously exposed to a 4 mT magnetic field. The orientation of the chains was normal to the ultrasound wave propagation (Z-axis). Secondly, experiment 2 also studied the QUS parameter variations in a horizontal magnetic field. This experiment probed the steady state of the horizontally aligned beads for different magnetic field intensities. Thirdly, in experiment 3, the phantom was placed in a vertical coil that generated a magnetic field (Figure 4). The magnetic field was parallel to the ultrasound wave propagation. This experiment probed the steady state of the vertically aligned beads for different magnetic field intensities.

The observed bead dynamics and the QUS parameter variations are related to previous

expectations (subsection II C 3). The actual bead dynamics and the physical meaning of each parameter are discussed in the light of the three experiments.

A. Beads dynamics

The microphotographs captured at different times revealed the existence of a 2-second transitional regime when the beads are instantaneously exposed to a magnetic field. In this first regime, the beads are moving and organizing themselves into chains. Then, the establishment of a steady state was observed, characterized by nearly immobile beads. In this steady state, the spatial pattern drawn by the beads does not correspond to the long equidistant chains that were initially expected since discontinuous chains of variable length appear. The heterogeneities of the external magnetic field and the non-uniform spatial distribution of the beads in their initial state (*e.g.*, the existence of bead aggregates with no magnetic field) could explain this observation.

B. The coherent-to-diffuse ratio

The coherent-to-diffuse ratio k_{hk} shows an increase during the transitional regime in experiment 1 (Figure 7, h), probably reflecting the increasing degree of structure inside the phantom solution. In the scalar approximation where the scattering is restricted to the Z-axis, the coherent signal could emanate from the periodicity of the spatial positions of the short chains, resulting from a regular repulsive distance. Interestingly, this hypothesis is supported by the microphotograph at $t = 4$ s (Figure 5, b) where repulsive distances about

two times the bead diameter can be observed. As the beads transition into the steady state, a decrease in the coherent-to-diffuse ratio k_{hk} was reported. To explain this phenomenon, a hypothesis is formulated below, in the light of the experiment 2.

In experiment 2, the coherent-to-diffuse ratio k_{hk} exhibit a slight decrease as the magnetic field increases and show a striking drop to near-zero values after 15 mT (Figure 8, h). This could be explained by the chain depopulation for a given resolution cell. Indeed, in a 2D approximation, the resolution cells is a rectangle that is about 26 µm along the Z axis, and 173 µm along the lateral direction. In the experiments 1 and 2, the chains are horizontal. Thus, a given resolution cell could encompass a single chain at maximum if the repulsive distance is greater than 26 µm (Figure 10, a). Interestingly, the steady-state microphotograph at 19 mT (Figure 5, e) supports this hypothesis by showing repulsive distances larger than 26 µm. As a result, in a scalar approximation where the scattering is strictly limited to occur along the Z axis, the large scatterers exhibit the same spatial positions along the Z axis and are therefore unable to generate interferences because of periodic spacings in this direction. In brief, only incoherent backscattering signals could emanate from an isolated horizontal chain in this configuration. Consequently, the coherent-to-diffuse ratio k_{hk} could exhibit an important decrease as the repulsive distances exceed the height of the resolution cell.

This hypothesis could also be applied to explain the steady-state decrease in k_{hk} mentioned in the first paragraph, in the time experience. Interestingly, the repulsive distances increase as a function of the time for a given magnetic field intensity, as revealed by the

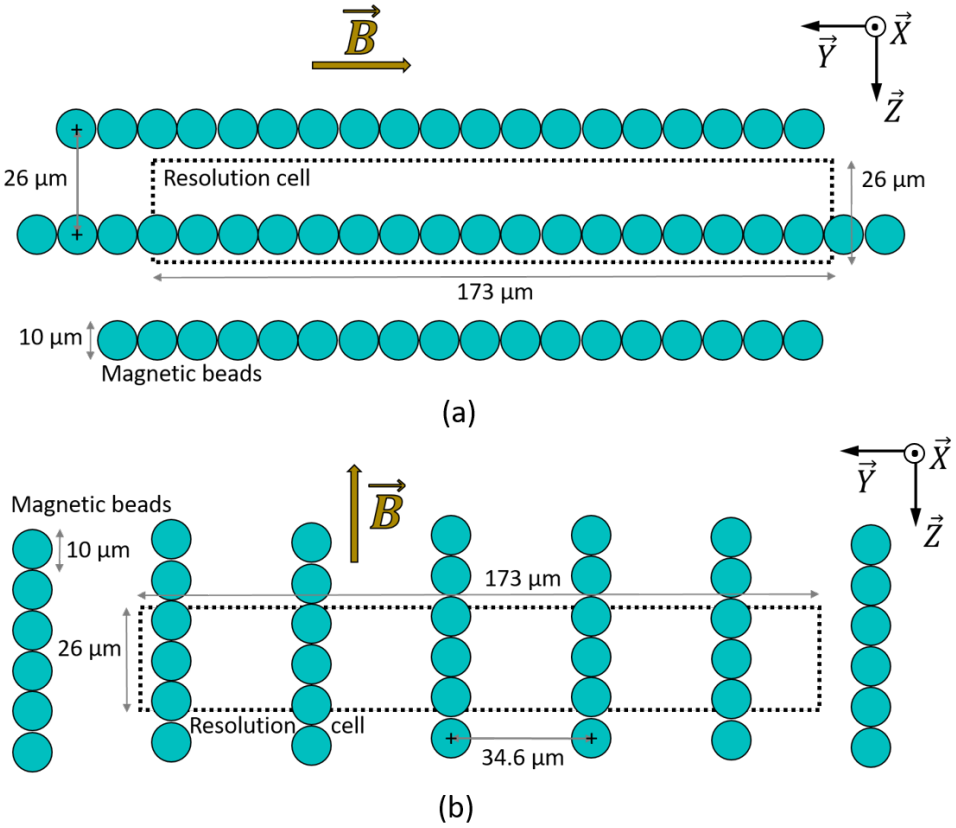

FIG. 10. 2D geometrical considerations. (a) Horizontal configurations. As the repulsive distances exceed the height of the resolution cell, the resolution cell may encompass one chain at maximum. (b) Vertical configuration. As the distance between the chains exceeds a critical repulsive distance ($173/5 = 34.6$ µm), the number of beads per resolution at maximum could not be greater than the one in the horizontal configuration. In both schemes, the scaling is maintained.

505 microphotographs at $t = 4$ s and $t = 9$ s (Figure 5, b and d). As the chains depopulate the
506 resolution cell, incoherent scattering could become predominant, thus justifying the time
507 variations of k_{hk}.

508 In the experiment 3, a broad range of k_{hk} values was observed for each magnitude of
509 the vector field $\|\vec{B}\|$ (Figure 9, h). This variability in data distribution complicates the

analysis of its evolution. However, no increase can be observed as it was predicted. This result could show that the scalar approximation in which the scattering is restricted to the Z-axis may be limited in this vertical configuration. Indeed, a coherent signal emanating from the periodic spacing (*i.e.*, one bead diameter) of the microspheres along the Z-axis was expected. Incoherent competing scattering signals originating from other directions may mask this coherent component, therefore preventing an increase in the coherent-to-diffuse signal ratio k_{hk}.

In summary, in the horizontal configurations, the effects of regular repulsive distances could be reported in the transitional regime only. The steady states potentially showed that the resolution cells tend to encompass individual chains, making the incoherent scattering predominant in this regime. Under these hypotheses that are supported by microphotographs, the coherent-to-diffuse signal ratio accurately reflected the spatial organization of the scatterers.

C. The Nakagami and the scatterer clustering QUS parameters

In experiment 1, α_{nak} exhibits an increase during the transitional regime from $\alpha_{nak} \approx 1.01$ to $\alpha_{nak} \approx 1.04$ (Figure 7, d), probably indicating an increasing number of scatterers per resolution cell and the early chain formations. However, the Nakagami parameter α_{nak} subsequently decreases down to $\alpha_{nak} \approx 0.97$ and reaches a level lower than that observed at the beginning, suggesting a lower number of scatterers per the resolution cell. To justify this observation, we can hypothesize that the contiguous microspheres act as larger scatterers in the steady state. In other words, the scattering of beads from the same chain could be mod-

eled by chains of grouped beads. As a result, the effective scatterer number density would decrease while the actual bead number density would remain mostly unchanged. This hypothesis could justify the observed decrease in the Nakagami parameter α_{nak}. If the previous assertion is true, this phenomenon is also expected to manifest as changes in the effective scatterer diameters (ESD). Interestingly, this hypothesis is supported by the observed slope variations, which is negatively correlated to the ESD (Lizzi *et al.*, 1988). Indeed, the slope S showed an important decrease as the beads transitioned into their steady state (Figure 7, a), probably indicating a notable increase in the ESD.

In the experiment 2, the Nakagami parameter α_{nak} decreases (Figure 8, d) with an increasing magnetic field. Similarly, the scatterer clustering QUS parameter μ_{hk} variations follow the same trend for the three strongest magnetic intensities (Figure 8, g). Interestingly, this could be explained following the same hypothesis mentioned above: the effective scatterers are larger but fewer for a given resolution cell. Indeed, the microphotographs at $\|\vec{B}\| = 4$ mT and $\|\vec{B}\| = 19$ mT (Figure 5, d, e) show that longer chains appear when $\|\vec{B}\|$ increases. As a result, the short chains that potentially represent the smallest ESD may become less numerous, therefore increasing the ESD values. Similarly to what was observed before, the decrease in the slopes reported in the experiment 2 may also support this assumption.

In the vertical steady state experiment, the Nakagami parameter α_{nak} and the scatterer clustering QUS parameter μ_{hk} decrease (Figure 9, d, g) with an increasing magnetic field. However, the slope S increases as the magnetic field increases, except at 8 mT. Indeed, less consideration can be attributed to this data point given the low corresponding R^2 co-

efficients. Therefore, it can be reasonably assumed that the slope S exhibits an opposite trend to the ones observed in experiments 1 and 2. Since we assumed that the previous decreases in slope values reflected an increase in ESD, the increase reported here cannot support the same conclusion regarding the ESD. Thus, the hypothesis of larger but fewer scatterers per resolution cell cannot be made here. Alternatively, this phenomenon could be explained by the scatterer (*i.e.*, bead) depopulation within a given resolution cell due to the repulsive distances between the chains. This hypothesis arises from the specific rectangular geometry of the resolution cell which exhibits a lateral resolution about 7 times longer than its axial resolution. Indeed, in this experiment, a given resolution cell "sees" fragments (*i.e.*, 3 magnetic beads at maximum) of parallel vertical chains, as opposed to the horizontal configurations, where a resolution cell can encompass longer horizontal chains (17 magnetic beads at maximum). Figure 10 (b) illustrates these geometrical considerations in a 2D approximation. Given that 3 beads per chain are included in the resolution cell, the number of beads per resolution cell at maximum cannot be greater than the one in the horizontal configuration if the distance between the chains exceeds the critical repulsive distance of $173/5 = 34.6$ µm. Indeed, $3 \times 5 = 15$ beads at maximum would be encompassed in a 2D resolution cell in the vertical configuration for this specific repulsive distance. The number of beads at maximum then decreases as the repulsive distance increases. Interestingly, the microphotograph of magnetic beads at $t = 9$ s under 4 mT magnetic field intensity (Figure 5, d) reveals the presence of repulsive distances higher than 30 µm. The repulsive distances are likely to increase as the magnetic field intensity increases given the higher spacings observed in the microphotograph at 19 mT (Figure 5, e). Thus, the critical repulsive distance

may be exceeded as $\|\vec{B}\|$ exceeds 4 mT. In brief, in this vertical configuration, the scatterer depopulation due the the bead alignment may be more pronounced as the magnetic field increases above a certain threshold, in comparison to the horizontal configurations.

In summary, the beads aligned within one horizontal chain could act as larger but less numerous scatterers in comparison to individual beads randomly located. In the vertical configuration, the beads could depopulate a given resolution cell by forming distant vertical chains. Under these hypotheses supported by microphotographs and geometrical considerations, the estimated Nakagami QUS parameters α_{nak} and the scatterer clustering QUS parameters μ_{hk} effectively described the scatterer number density.

D. The intercept and the scaling parameters

In experiment 1, the observed increases in the intercepts I and the scaling parameters Ω_{nak} (Figure 7, b, e) could potentially reflect an increase in the incoherent BSC since the coherent signals vanish in the steady state. The incoherent BSC is defined as the product of the scatterer number density with the differential backscattering cross-section σ_b. To explain the increase in the incoherent BSC, the increasing scatterer density due to contiguous beads could have been a plausible hypothesis. However, the variations in the Nakagami and the clustering QUS parameters mentioned previously showed the opposite phenomenon. Alternatively, the increase in the incoherent BSC could be explained by the increase in the effective differential backscattering cross-section σ_b. Indeed, when the beads are aligned, the effective scatterers are likely to exhibit a strong geometrical anisotropy. Specifically, in this horizontal configuration, the effective scattering cross-sections could reflect the numer-

ous contiguous beads from the same chain. Thus, we hypothesize that the effects of the increasing differential backscattering cross-section are predominant and overcompensate for the scatterer depopulation for a given resolution cell.

In experiment 2, the intercept I and the scaling parameter Ω_{nak} increase as the magnetic field intensity increases (Figure 8, b, e). Similarly, this phenomenon could reflect an increase in the incoherent BSC since the coherent signals vanish in the steady state. As detailed in the previous paragraph, the effective differential backscattering cross-section may be higher when the beads are horizontally aligned in comparison to when the beads are randomly located.

Interestingly, the Ω_{nak} and the intercept I continuously increased as the magnetic field intensity increased. However, horizontal chains were already observed in the steady state for a low magnetic field intensity (Figure 5, d). Thus, the previous hypothesis may be insufficient to justify this observation. An additional mechanism could justify the continuous increase in the incoherent BSC when the beads are already aligned horizontally. To understand this phenomenon, we can hypothesize that the magnetic cohesion among the beads from the same chain could also contribute to the increases in the differential backscattering cross-section. In other words, the magnetic forces that maintain the scatterer's position in the steady state may increase the backscattering signal when the scatterer faces a disturbance (*i.e.*, an incident wave). We hypothesize that this effect could manifest as an increase in the relative impedance contrast γ_z.

One should note that the increase in the effective scattering cross section due to the horizontal geometrical alignment and the increase in the effective relative impedance contrast

could be concomitant. Similarly, we infer that the resulting increase in the incoherent BSC overcompensates for the scatterer depopulation in this experiment.

In the experiment 3, the scaling parameter Ω_{nak} decreases as the magnetic field increases (Figure 9, e). The intercept I denoted a decrease between extreme magnetic field intensity values (Figure 9, b). The hypothesis formulated above to justify the variations of the Nakagami QUS parameters in the vertical configuration could be applied here. In this case, the intercept I and Ω_{nak} would then reflect the decrease in the incoherent BSC and more specifically the scatterer depopulation within a given resolution cell. The increase in the effective relative impedance contrast due to the magnetic cohesion of the beads within one chain may also be present. However, this mechanism could manifest minor effects in comparison. Indeed, both the Nakagami QUS parameters α_{nak} and the scatterer clustering QUS parameter μ_{kh} exhibit a stronger decay at 11 mT in experiment 3 in comparison to one observed in experiment 2. This observation may suggest a more pronounced scatterer depopulation.

In summary, in the horizontal configuration, the intercept I and the scaling parameters could reflect the variations in the incoherent BSC and more specifically the increase in the effective differential backscattering cross-section. Experiment 1 showed that the geometrical horizontal alignment of the beads may contribute to this effect while experiment 2 potentially revealed the existence of a magnetic cohesion that could impact the effective relative impedance contrast. Experiment 3 may have shown a stronger scatterer depopulation when the beads are aligned vertically in comparison to horizontal chains.

This study presents some limitations that are discussed below:

Firstly, the microphotographs depicted the 2D dynamics of the beads, as they were in

motion within a droplet of solution applied to a microscope slide. As a result, the 3D bead dynamics may not have been fully captured. As an approximation, the microphotographs served as references to assume the scatterer's behavior in 3D. Thus, the QUS parameters may have reflected mechanisms that were not observed under the microscope and that could have been omitted as a result. One could note that the limited number of available microphotographs makes the quantitative analysis of the bead dynamics challenging (*e.g.* length of chains or repulsive distance as a function of time).

Secondly, the phase of the scattering waves was reduced to its projection along the vertical axis as part of a scalar approximation when discussing the evolutions of the coherent-to-diffuse ratio k_{kh} (section IV B). This assumption may have oversimplified the vectorial nature of scattering, specifically in experiment 3 where the expected coherent signal was not observed. A vectorial simulation tool could be developed to overcome these limitations.

Thirdly, the fast mechanical displacement of the mono-element transducer may have impacted the bead spatial organization and could have affected the bead scattering as a result. The beads exhibited a slow uniform vertical movement that resembles sedimentation (typically after 10 s) because the magnetic fields were not perfectly homogeneous. Therefore, the scanning speed was set to an in-between to allow gentle displacement that mitigates the effect of magnetic field heterogeneities. The use of a multi-element probe may overcome these limitations.

To our knowledge, no quantitative ultrasound study has previously leveraged the properties of superparamagnetic beads to analyze the ultrasound coherent scattering. We believe that this work paves the way toward a novel type of phantom design method. This ap-

proach could be of prime interest to validate theoretical scattering models in structured media. Additionally, it is noteworthy that the magnetic components are inexpensive and widely available (*e.g.* magnets or coil), therefore making our setup easily reproducible.

This study was limited to a uniform magnetic field. However, one could note that numerous magnetic field patterns could be achieved using different magnet configurations. For instance, Halbach cylinders consist of circular arrangements of solid magnets in which the magnetic field is confined within the cylinder (Bjørk *et al.*, 2008). Changing the direction of the magnetic moment of each magnet allows to obtain different field patterns. As a result, a great variety of chain organizations could be obtained and studied. Thus, this approach could be adapted to different applications, particularly within clinical settings.An illustrative example involves reproducing specific cellular structural organizations within magnetic phantoms to investigate their impact on ultrasound scattering. This methodology using phantoms may be relevant to develop new detection techniques for the pathological conditions that induce an abnormal cellular organization such as dysplasia, which is a pre-cancerous condition (Witt, 2003). In this case, the detection of structural effects may provide valuable diagnostic insights into the probed tissue. For instance, the collecting ducts of kidneys exhibit cuboidal epithelia, characterized by a highly organized layer of cells (Matz *et al.*, 1997). This tissue can turn malignant and lead to a collecting duct carcinoma, which is an aggressive form of kidney cancer (Dimopoulos *et al.*, 1993).

V. CONCLUSIONS

In conclusion, a new way to control the distribution of scatterers in a phantom using superparamagnetic beads was introduced to study structural effects on ultrasound scattering. Consistent hypotheses supported by microphotographs were formulated to describe the variations of QUS parameters according to their physical interpretation reported in the literature in the distinct configurations.

Bjørk, R., Bahl, C. R. H., Smith, A., and Pryds, N. (**2008**). "Optimization and improvement of halbach cylinder design," Journal of Applied Physics **104**(1).

Cristea, A., Collier, N., Franceschini, E., Mamou, J., Cachard, C., and Basset, O. (**2020**). "Quantitative assessment of media concentration using the homodyned k distribution," Ultrasonics **101**, 105986.

Destrempes, F., Porée, J., and Cloutier, G. (**2013**). "Estimation method of the homodyned k-distribution based on the mean intensity and two log-moments," SIAM journal on imaging sciences **6**(3), 1499–1530.

Dimopoulos, M., Logothetis, C., Markowitz, A., Sella, A., Amato, R., and Ro, J. (**1993**). "Collecting duct carcinoma of the kidney," British journal of urology **71**(4), 388–391.

Faran Jr, J. J. (**1951**). "Sound scattering by solid cylinders and spheres," The Journal of the acoustical society of America **23**(4), 405–418.

Franceschini, E., and Guillermin, R. (**2012**). "Experimental assessment of four ultrasound scattering models for characterizing concentrated tissue-mimicking phantoms," The Jour-

nal of the Acoustical Society of America **132**(6), 3735–3747, doi: 10.1121/1.4765072.

Garcia-Duitama, J., Chayer, B., Han, A., Garcia, D., Oelze, M. L., and Cloutier, G. (**2015**). "Experimental Application of Ultrafast Imaging to Spectral Tissue Characterization," Ultrasound in Medicine and Biology **41**(9), 2506–2519, doi: 10.1016/j.ultrasmedbio.2015.04.017.

Han, A., and O'Brien, W. (**2015**). "Structure function for high-concentration biophantoms of polydisperse scatterer sizes," IEEE Transactions on Ultrasonics, Ferroelectrics, and Frequency Control **62**(2), 303–318, doi: 10.1109/TUFFC.2014.006629.

Huang, L., Donohue, K., Genis, V., and Forsberg, F. (**2000**). "Duct detection and wall spacing estimation in breast tissue," Ultrasonic imaging **22**(3), 137–152.

Insana, M. F., Wood, J. G., and Hall, T. J. (**1992**). "Identifying acoustic scattering sources in normal renal parenchyma in vitro by varying arterial and ureteral pressures," Ultrasound in Medicine & Biology **18**(6), 587–599, https://www.sciencedirect.com/science/article/pii/030156299290073J, doi: https://doi.org/10.1016/0301-5629(92)90073-J.

Kauati, A., Pereira, W. C. d. A., and Campos, M. L. R. (**2018**). "Mean scatterer space estimation from ultrasound signals combining singular spectral analysis and entropy," Research on Biomedical Engineering **34**, 157–165.

Kuc, R., and Schwartz, M. (**1979**). "Estimating the acoustic attenuation coefficient slope for liver from reflected ultrasound signals," IEEE Transactions on Sonics and Ultrasonics **26**(5), 353–361.

723 Lizzi, F. L., King, D. L., Rorke, M. C., Hui, J., Ostromogilsky, M., Yaremko, M. M., Feleppa,
724 E. J., and Wai, P. (**1988**). "Comparison of theoretical scattering results and ultrasonic data
725 from clinical liver examinations," Ultrasound in medicine & biology **14**(5), 377–385.
726 Lizzi, F. L., Ostromogilsky, M., Feleppa, E. J., Rorke, M. C., and Yaremko, M. M. (**1987**).
727 "Relationship of ultrasonic spectral parameters to features of tissue microstructure," IEEE
728 transactions on ultrasonics, ferroelectrics, and frequency control **34**(3), 319–329.
729 Mamou, J., Coron, A., Oelze, M. L., Saegusa-Beecroft, E., Hata, M., Lee, P., Machi, J.,
730 Yanagihara, E., Laugier, P., and Feleppa, E. J. (**2011**). "Three-dimensional high-frequency
731 backscatter and envelope quantification of cancerous human lymph nodes," Ultrasound in
732 Medicine and Biology **37**(3), 345–357, doi: 10.1016/j.ultrasmedbio.2010.11.020.
733 Matz, L. R., Latham, B. I., Fabian, V. A., and Vivian, J. B. (**1997**). "Collecting duct
734 carcinoma of the kidney: a report of three cases and review of the literature," Pathology
735 **29**(4), 354–359.
736 Muleki-Seya, P., Guillermin, R., Guglielmi, J., Chen, J., Pourcher, T., Konofagou, E.,
737 and Franceschini, E. (**2016**). "High-Frequency Quantitative Ultrasound Spectroscopy of
738 Excised Canine Livers and Mouse Tumors Using the Structure Factor Model," IEEE
739 Transactions on Ultrasonics, Ferroelectrics, and Frequency Control **63**(9), 1335–1350, doi:
740 10.1109/TUFFC.2016.2563169.
741 Muleki-Seya, P., Han, A., Andre, M. P., Erdman Jr, J. W., and O'Brien Jr, W. D. (**2018**).
742 "Analysis of two quantitative ultrasound approaches," Ultrasonic imaging **40**(2), 84–96.
743 Narayanan, V. M., Molthen, R. C., Shankar, P., Vergara, L., and Reid, J. (**1997**). "Studies
744 on ultrasonic scattering from quasi-periodic structures," IEEE transactions on ultrasonics,

ferroelectrics, and frequency control **44**(1), 114–124.

Oelze, M. L., and Mamou, J. (**2016**). "Review of Quantitative Ultrasound: Envelope Statistics and Backscatter Coefficient Imaging and Contributions to Diagnostic Ultrasound," IEEE Transactions on Ultrasonics, Ferroelectrics, and Frequency Control **63**(2), 336–351, doi: 10.1109/TUFFC.2015.2513958.

Pereira, W. C., Abdelwahab, A., Bridal, S. L., and Laugier, P. (**2002**). "Singular spectrum analysis applied to 20mhz backscattered ultrasound signals from periodic and quasi-periodic phantoms," Acoustical Imaging 239–246.

Rosado-Mendez, I. M., Carlson, L. C., Hall, T. J., and Zagzebski, J. A. (**2013**). "A multitaper generalized spectrum technique for detection of periodic structures in tissue: Comparison with conventional methods," in *2013 IEEE International Ultrasonics Symposium (IUS)*, IEEE, pp. 433–436.

Saha, R. K., and Kolios, M. C. (**2011**). "Effects of cell spatial organization and size distribution on ultrasound backscattering," IEEE Transactions on Ultrasonics, Ferroelectrics, and Frequency Control **58**(10), 2118–2131, doi: 10.1109/TUFFC.2011.2061.

Sommer, F. G., Joynt, L. F., Carroll, B. A., and Macovski, A. (**1981**). "Ultrasonic characterization of abdominal tissues via digital analysis of backscattered waveforms.," Radiology **141**(3), 811–817.

Wagner, R. F., Brown, D. G., and Hall, T. J. (**1990**). "Describing small-scale structure in random media using pulse-echo ultrasound," Journal of the Acoustical Society of America **87**(1), 179–192, doi: 10.1121/1.399283.

766 Weng, L., Reid, J. M., Shankar, P. M., Soetanto, K., and Lu, X.-M. (**1992**). "Nonuniform
767 phase distribution in ultrasound speckle analysis. i. background and experimental demon-
768 stration," IEEE transactions on ultrasonics, ferroelectrics, and frequency control **39**(3),
769 352–359.

770 Witt, D. R. (**2003**). "Dysmorphology," in *Encyclopedia of the Neurological Sciences*, edited
771 by M. J. Aminoff and R. B. Daroff (Academic Press, New York), pp. 56–62, https:
772 //www.sciencedirect.com/science/article/pii/B012226870900006X, doi: https://
773 doi.org/10.1016/B0-12-226870-9/00006-X.

774 Yao, L. X., Zagzebski, J. A., and Madsen, E. L. (**1990**). "Backscatter Coefficient Measure-
775 ments Using a Reference Phantom to Extract Depth-Dependent Instrumentation Factors,"
776 Ultrasonic Imaging **12**(1), 58–70, doi: 10.1177/016173469001200105.

777 Zhou, Z., Wu, W., Wu, S., Jia, K., and Tsui, P.-H. (**2017**). "A review of ultrasound tissue
778 characterization with mean scatterer spacing," Ultrasonic imaging **39**(5), 263–282.